Unraveling microstrain-promoted structural evolution and thermally driven phase transition in c-Sc$_2$O$_3$ nanocrystals at high pressure

Yongtao Zou [1,2,*] Mu Li [1] Wei Zhang,[3] Cangtao Zhou,[1,†] Tony Yu,[4] Hongbin Zhuo,[1] Yanbin Wang,[4] Yusheng Zhao,[5] Shuangchen Ruan,[1,‡] and Baosheng Li[2]

[1]*College of Engineering Physics, and Center for Advanced Material Diagnostic Technology, Shenzhen Technology University, Shenzhen 518118, China*
[2]*Mineral Physics Institute, State University of New York, Stony Brook, New York 11790, USA*
[3]*School of Science, Southwest University of Science and Technology, Mianyang, Sichuan 610064, China*
[4]*Center for Advanced Radiation Sources, The University of Chicago, Chicago, Illinois 60637, USA*
[5]*Academy for Advanced Interdisciplinary Studies, and Department of Physics, Southern University of Science and Technology (SUSTech), Shenzhen 518055, China*

Here, we report an irreversible cubic-to-monoclinic structural transition in cubic c-Sc$_2$O$_3$ nanocrystals which occur at pressures above ∼8.9 GPa upon nonhydrostatic compression in association with a pronounced volume collapse. This phase-transition–induced anomaly is further confirmed by our experimental Raman spectroscopy measurements and theoretical predictions. After annealing, however, this high-pressure monoclinic m-Sc$_2$O$_3$ phase undergoes a reversible back-transformation to the cubic counterpart at ∼1123 K and 9.0 GPa. Our observed transition pressure of ∼8.9 GPa for the cubic-to-monoclinic structural evolution is significantly lower than that from the previously diamond-anvil-cell–based hydrostatic x-ray experiments because of the existence of internal microscopic stress and/or high-stress concentration in the specimen caused by grain-to-grain contacts upon nonhydrostatic compression, which promoted the cubic-to-monoclinic structural transition. Moreover, we have reported new thermoelastic properties of c-Sc$_2$O$_3$ nanocrystals at simultaneous high-pressure and high-temperature conditions. These findings/results may have significant implications for the design of phase-switching devices and for the exploration of the structural relationship among sesquioxides for their uses in extreme environments.

I. INTRODUCTION

Scandium oxide (Sc$_2$O$_3$), as an important rare-earth sesquioxide, has recently attracted considerable attention for its potential applications in nuclear engineering, high-temperature ceramics, photonic and optoelectronic devices, and laser optical coatings because of its unique physical and chemical properties, such as high refractive index, high damage threshold, high ultraviolet cutoff, and good chemical stability [1–4].

At ambient conditions, scandia crystallizes into a cubic bixbyite-type structure (c-Sc$_2$O$_3$; space group:$Ia\bar{3}$) with six-coordinated cations in Fig. 1(a). This crystal structure is typical for many rare-earth sesquioxides, suggesting that the high-pressure behavior of c-Sc$_2$O$_3$ may be similar to that of lanthanide sesquioxides [5–7]. It has been reported that Sc$_2$O$_3$ remains in a cubic structure at temperatures up to its melting point at ambient pressure without any observable phase transitions [8]. By contrast, the previous x-ray diffraction and Raman spectroscopy measurements showed that the cubic

bixbyite-structured Sc$_2$O$_3$ transformed into a monoclinic phase (m-Sc$_2$O$_3$, space group: $C2/m$) at pressures ranging from 28–36 GPa at room temperature [9,10], where the six- and seven-coordinated sites were occupied by the Sc cations [Fig. 1(b)]. However, the recent theoretical calculations of different Gibbs free energy under high pressure showed that the cubic c-Sc$_2$O$_3$ transformed into the monoclinic polymorph at 15 GPa and then changed into a Gd$_2$S$_3$ phase at 18 GPa [11]. On the other hand, high-pressure–temperature experiments by Reid and Ringwood [12] suggested that this cubic-to-monoclinic transition occurred at much lower pressures of 10–15 GPa when heating up to 1000 °C. With further increase of pressure and temperature up to ∼19 GPa and 2000 K, the phase transition pathway of Sc$_2$O$_3$ was proposed from the cubic-to-monoclinic structure then to a hexagonal phase (space group:$P\bar{3}m$1) [13]. However, this structural phase transition was not observed by the previous shock compression experiments at pressures of 20 and 40 GPa, only exhibiting a slight broadening in the x-ray diffraction peaks compared with those of the initial c-Sc$_2$O$_3$ phase [14].

In addition to the structural stability, thermoelastic properties are also important parameters for understanding the behavior and physical properties of c-Sc$_2$O$_3$ under high pressure. The bulk modulus/compressibility of c-Sc$_2$O$_3$ has been studied by several static-compression experiments and

*zouyongtao@sztu.edu.cn
†zcangtao@sztu.edu.cn
‡scruan@sztu.edu.cn
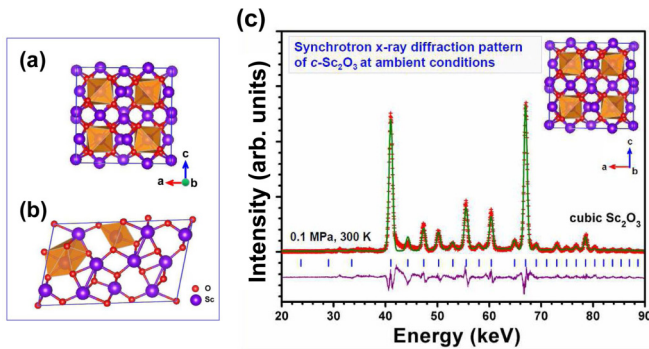
FIG. 1. Crystal structures of (a) cubic bixbyite-type structured Sc_2O_3 (c-Sc_2O_3; space group:$Ia\bar{3}$; $Z = 16$) with six-coordinated scandium (Sc) cations and (b) high-pressure phase of monoclinic Sc_2O_3 structure (m-Sc_2O_3; space group: $C2/m$; $Z = 6$), where the six- and seven-coordinated sites are occupied by the Sc cations. Blue and red spheres represent Sc and oxygen (O) ions, respectively. (c) Refined energy-dispersive x-ray diffraction pattern of c-Sc_2O_3 nanocrystals at ambient conditions, showing a cubic structure (space group:$Ia\bar{3}$).

first-principles calculations; however, the reported values are quite scattered with significant discrepancies, ranging from 156 to 197 GPa [15–17]. Earlier experimental studies on the elastic constants of single-crystal Sc_2O_3 yielded the $B_{VRH} = 197$ GPa [15]. Dole *et al.* [16] have studied the effect of porosity on the elastic moduli in c-Sc_2O_3, yielding the bulk modulus of $\sim$156 GPa for a full dense bulk c-Sc_2O_3 sample. Recently, Yusa *et al.* [13] and Liu *et al.* [9] have performed experimental x-ray diffraction studies on the stability and compressibility of scandia at high pressure and room temperature in a diamond-anvil cell (DAC), giving $B_{T0} = 189(7)$ GPa and 154(5) GPa, respectively.

Despite its importance, previous studies on the high-pressure behavior of c-Sc_2O_3 are still rather scarce, and there is a lack of simultaneous high-pressure and high-temperature research on its structural stability and thermoelasticity. Here, we have performed a synchrotron *in situ* x-ray diffraction study on the structural evolution and thermoelasticity of c-Sc_2O_3 nanocrystals at simultaneous high-pressure and high-temperature conditions in a multi-anvil high-pressure apparatus, complemented with high-pressure Raman spectroscopy measurements and first-principles density functional theory (DFT) calculations. For the first time, we report a reversible structural switching between the microstrain-promoted structural changes and thermal-driven phase transition, as well as the thermoelasticity of c-Sc_2O_3 nanocrystals at simultaneously high pressure-temperature (P-T) conditions. These findings/results are not only of great importance in understanding the thermoelasticity of Sc_2O_3, but also may have significant implications for the design of phase-switching devices and the exploration of the structural relationship among sesquioxides for their uses at extreme conditions.

II. EXPERIMENTAL AND THEORETICAL DETAILS

A. Synchrotron x-ray diffraction

The starting material of c-Sc_2O_3 powder used for the current experiments was commercially available (Rare-Chem

Hi-Tech Co. Ltd., China). Synchrotron *in situ* high P-T x-ray diffraction experiments were performed in a large-volume press at GSECARS (13-IDD) at the Advanced Photon Source, Argonne National Laboratory. Details of the experimental setup have been described elsewhere [18–20]. Briefly, the MgO octahedron was employed as a pressure-transmitting medium. In this paper, we used a mixture of NaCl + h-BN (1:10 by weight) as an internal pressure marker to determine the cell pressures and used graphite as a furnace/heater. X-ray diffraction patterns for both the specimen and pressure marker were collected using a solid-state detector at a diffraction angle of $2\theta \approx 6.09°$. Peak positions and extraction of lattice parameters of the Sc_2O_3 specimen and NaCl pressure marker were refined by reducing full diffraction patterns following the Le Bail method with the multiphase profile-fitting technique implemented in the EXPGUI/GSAS software package [21,22]. Precisions in unit-cell volumes for both the sample and the pressure marker were determined from the Le Bail refinement of x-ray diffraction profiles. The cell pressures were calculated based on the Decker's equation of state (EOS) of NaCl [23]. Temperatures were monitored by a $W_{97}Re_3$-$W_{75}Re_{25}$ thermocouple. Uncertainties in temperature measurements due to the gradient in the furnace were within ± 50 K. During the current experiments, the Sc_2O_3 specimen was initially compressed up to a desired pressure at room temperature then heated to the maximum temperature of $\sim$1123 K and stepwise cooled down to room temperature of $\sim$300 K. The same procedure was repeated several times at progressively low pressures. Along the experimental P-T paths, x-ray diffraction data were collected for both the sample and NaCl pressure marker at selected P-T conditions.

B. Raman spectroscopy measurements

High-pressure Raman spectroscopy measurements on c-Sc_2O_3 nanocrystals were performed at room temperature in a DAC. No pressure-transmitting medium was used in this experiment. Cell pressures were determined by measuring the shift of fluorescence peaks of ruby at high pressure [24]. The current Raman measurements were carried out by means of a Raman spectrometer with a laser wavelength of 514 nm (Ar) at a power level of 100 mW.

C. First-principles calculations

In our theoretical calculations, the interactions between electrons and ionic cores were treated with the ultrasoft pseudopotentials, and the exchange-correlation potentials were done by generalized gradient approximation of DFT [25,26]. During the pseudopotentials calculations, the valence electron densities were defined by Sc ($3s3p3d4s$) and O ($2s2p$). The electronic wave functions were expanded in a plane-wave basis set with a cutoff energy of 600 eV. The Monkhorst-Pack k-points were selected to be $4 \times 4 \times 4$. Hydrostatic pressures were realized within the variable cell approaches by employing the Parrinello-Rahman method [27]. At each target external pressure, a full optimization of the cell structure was performed. All total energy electronic structure calculations were carried out by Cambridge Serial Total Energy Package code [28].
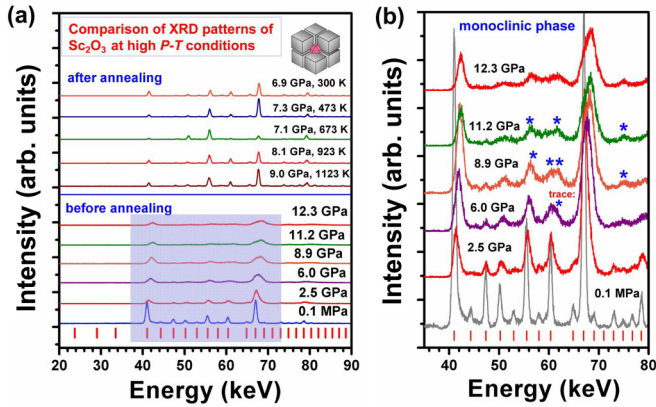
FIG. 2. (a) Representative x-ray diffraction patterns for Sc_2O_3 nanocrystals under nonhydrostatic compression in comparison with those at simultaneous high pressure and high temperature. (b) Enlarged x-ray diffraction patterns for Sc_2O_3 nanocrystals under nonhydrostatic high-pressure conditions (cold compression), showing the appearance of new peaks resulting from the pressure-induced cubic-to-monoclinic phase transition. The labeled blue asterisks are the new peaks (or trace) from monoclinic structured Sc_2O_3. The red tick marks correspond to the peak positions of c-Sc_2O_3.

III. RESULTS AND DISCUSSION

Le Bail refinement of energy-dispersive *in situ* x-ray diffraction pattern of the starting material of Sc_2O_3 nanocrystals at ambient conditions is shown in Fig. 1(c). Clearly, all diffraction peaks can be well-indexed to a cubic structure (space group:$Ia\bar{3}$, No. 206, $Z = 16$), yielding the lattice parameter of $a_0 = 9.8476(5)$ Å and unit-cell volume of $V_0 = 954.98 \pm 0.13$ Å^3. These results are in excellent agreement with the recent angle-dispersive x-ray diffraction experimental results of $a_0 = 9.846$ Å and $V_0 = 954.56$ Å^3 [17] and the theoretical results of $a_0 = 9.830$ Å [29] and $V_0 = 953.92$ Å^3 [10], but ∼0.6% and ∼1.6% smaller than the previous compression experimental results of $a_0 = 9.905(3)$ Å and $V_0 = 971.84(16)$ Å^3 [9], respectively.

Representative synchrotron *in situ* x-ray diffraction patterns of c-Sc_2O_3 nanocrystals upon nonhydrostatic compression are shown in Fig. 2(a), together with those after annealing at simultaneous high-pressure and high-temperature conditions. For close observations, the enlarged x-ray diffraction patterns within 35–80 keV upon nonhydrostatic compression are shown in Fig. 2(b). With increasing pressure, the relative intensity of the major peaks of the cubic c-Sc_2O_3 became weak, indicating the changes of atomic positions in c-Sc_2O_3. Moreover, the diffraction peaks for c-Sc_2O_3 start to broaden and new x-ray peaks occur at pressures above ∼8.9 GPa in Fig. 2(b). These results indicate that a pressure-induced phase transition in c-Sc_2O_3 occurred and formed a new structure at pressures above ∼8.9 GPa. This new phase is referred to as the monoclinic structure by Liu *et al.* [9] and Reid and Ringwood [12]. Clearly, the current transition pressure ($P_{tr} \approx 8.9$ GPa) for cubic-to-monoclinic structural transition is significantly lower than the values of around 10 GPa after heating up to 1600 K [12] and of 28–36 GPa by hydrostatic compression experiments in a DAC [9,10]. We propose the reason for the relatively lower P_{tr} is attributed to the existence of internal
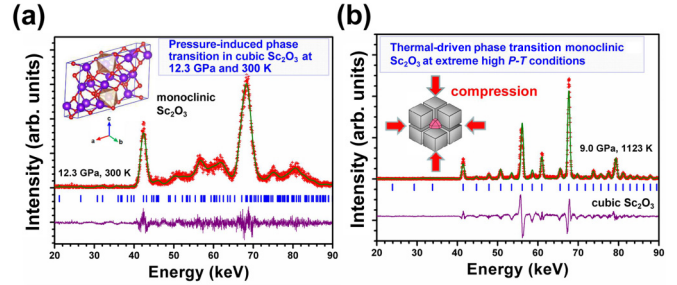
FIG. 3. (a) Synchrotron *in situ* x-ray diffraction pattern of monoclinic m-Sc_2O_3 at 12.3 GPa and 300 K upon compression. (b) *In situ* x-ray diffraction pattern of c-Sc_2O_3 at 9.0 GPa and 1123 K, as back-transformed from the high-pressure monoclinic phase of m-Sc_2O_3 after annealing. Red crosses and green curves denote the observed and calculated profiles, respectively. The difference curve between the observed and the calculated profiles is shown in brown. The blue tick marks correspond to the peak positions.

microscopic stress or high-stress concentration in the specimen caused by grain-to-grain contacts upon nonhydrostatic compression. On the other hand, after annealing of the formed monoclinic m-Sc_2O_3 phase at ∼1123 K and 9.0 GPa, we find that the monoclinic Sc_2O_3 nanocrystals undergo a reversible reconstructive phase transition and transform back to the cubic Sc_2O_3, persisting to the ambient conditions. These results indicate a reversible switching between the cubic and monoclinic Sc_2O_3 driven by temperatures and pressures.

To further determine the crystal structure of this high-pressure new phase, the refinement of a representative x-ray diffraction pattern of Sc_2O_3 at 12.3 GPa is shown in Fig. 3(a), yielding a monoclinic structure of m-Sc_2O_3 (space group: $C2/m$). As seen in an inset of Fig. 3(a) or Fig. 1(b), the high-pressure phase of m-Sc_2O_3 has different atomic arrangements, containing three nonequivalent point symmetry Cs coordination Sc^{3+} ions within the lattice of O^{2-} ions and with O atoms located at Wyckoff positions $4i$ and $2b$. The lattice parameters of the newly monoclinic phase refined by this space group were $a = 12.956(5)$ Å, $b = 3.393(2)$ Å, $c = 7.793(3)$ Å and $\beta = 103.16(2)°$, and the unit-cell volume was $V_0 = 333.54(16)$ Å^3. These values are in good agreement with those from previous high-pressure or high-temperature studies [9,12]. As shown in Fig. 3(b), the cubic structure of Sc_2O_3 can be clearly identified from the Le Bail refinement of the x-ray diffraction pattern of metastable m-Sc_2O_3 after annealing at 1123 K and 9.0 GPa, revealing a reconstructive phase transition from the monoclinic structure to a cubic one.

Figure 4(a) shows the unit-cell volumes and lattice parameters of c-Sc_2O_3 and m-Sc_2O_3 as a function of pressure as derived from the refinements of the current synchrotron x-ray diffraction data. Clearly, the changes in unit-cell volumes and lattice parameters that resulted from the cubic-to-monoclinic phase transition are pronounced, reaching the volume-per-formula collapse $\Delta(V/Z)$ of ∼1.5% at 11.2 GPa, which is strong evidence for the first-order phase transition upon nonhydrostatic compression.

It is well known that the diffraction peak width is primarily determined by the instrument contribution, crystallite size effect, and inhomogeneous strain (microstrain), as
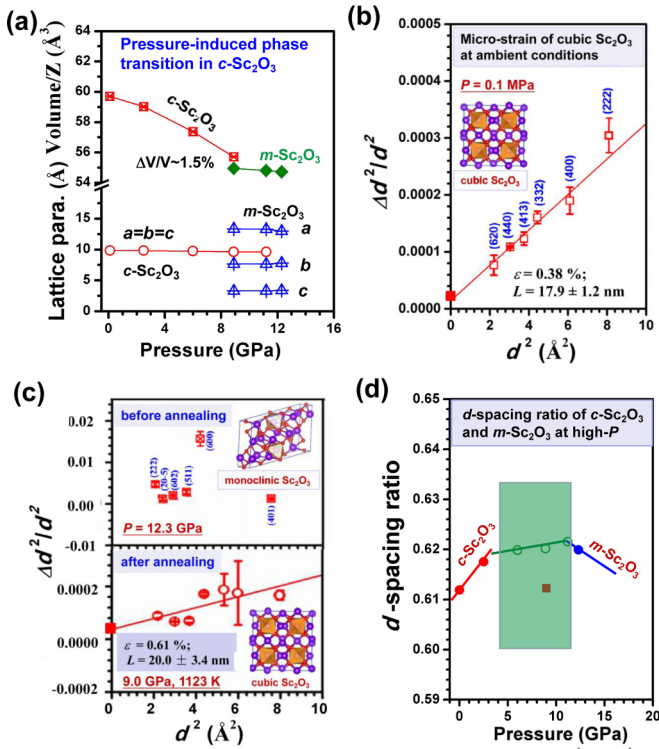
FIG. 4. (a) Lattice parameters and volumes per formula for Sc_2O_3 nanocrystals as a function of pressure (upon cold compression), showing a pronounced pressure-induced volume collapse at pressures above ~ 8.9 GPa resulting from the cubic-to-monoclinic phase transition. The straight color lines are guides to the eyes. (b) Plot of $\Delta d_{obs}^2/d^2$ versus d^2 according to the modified Williamson-Hall equation for c-Sc_2O_3 nanocrystals at ambient conditions. It illustrates the determination of apparent strain and crystallite/grain size from the intercept and slope of the fitted linear lines. The raw data of c-Sc_2O_3 are shown as the open red squares, and the solid red square denotes the extrapolated value. (c) Plot of $\Delta d_{obs}^2/d^2$ versus d^2 for m-Sc_2O_3 at 12.3 GPa (top) in comparison with the results at the highest P-T conditions of 9.0 GPa and 1123 K for c-Sc_2O_3 (bottom). (d) Representative d-spacing ratio of c-Sc_2O_3 as a function of pressure compared with those for metastable m-Sc_2O_3 at 12.3 GPa and the reconstructive c-Sb_2O_3 after annealing at 1123 K and 9.0 GPa, indicating an apparent microstrain-promoted reconstructive phase transition. The straight (dash) lines are guides to the eyes.

described in the modified Williamson-Hall equation [30,31] of $\Delta d_{obs}^2/d^2 = (\varepsilon^2 + \Delta d_{ins}^2/d^2/d^2) + (1/d^2$, where Δd_{obs} and Δd_{ins} are the observed peak width and the peak width from the instrument contribution, respectively, d is the d spacing of a given lattice plane, and L is the crystallite size. Clearly, this equation is a typical $Y = a + bX$ plot. Therefore, we can derive the apparent microstrain $\varepsilon_{apparent}^2 = (\varepsilon^2 + \Delta d_{ins}^2/d^2/d^2)$ as well as the average crystallite size (L) from the ordinate intercept and the slope of the $\Delta d_{obs}^2/d^2$ versus d^2 plot, respectively.

Figure 4(b) shows the separation of crystallite size (L) and microstrain (ε) contributions in the plot of $\Delta d_{obs}^2/d^2$ against d^2 for the starting material of c-Sc_2O_3 at ambient conditions, yielding the apparent microstrain of $\sim 0.38\%$ due to the instrument contribution, and the average grain/crystallite size of ~ 18 nm, which is confirmed by our Scanning Electron

Microscopy (SEM) observation in the Supplemental Material, Section I (SI) [32]. For comparison, the normalized peak-width $\Delta d_{obs}^2/d^2$ against d^2 for high-pressure m-Sc_2O_3 phase at 12.3 GPa (top) and reconstructive c-Sc_2O_3 nanocrystals after annealing at 1123 K and 9.0 GPa (bottom) are shown in Fig. 4(c). Noticeably, the observed raw data ($\Delta d_{obs}^2/d^2$ vs d^2) for m-Sc_2O_3 become more scattered upon nonhydrostatic compression than those for c-Sc_2O_3 at ambient conditions. An example of such derivation from x-ray diffraction data of m-Sc_2O_3 at 12.3 GPa is illustrated in Fig. 4(c) (top). Clearly, a simple straight line cannot be drawn through the apparent variation in lattice strains according to different (hkl) diffraction planes to derive the microstrain and grain size from the plot, indicating the fact that different crystal planes of m-Sc_2O_3 at a high pressure of 12.3 GPa are not strained the same as each other. We found that the strain values ($\varepsilon = \Delta d/d$) due to the grain-to-grain contacts of metastable high-pressure phase for m-Sc_2O_3 are several times higher than that for c-Sc_2O_3 at ambient conditions [see Figs. 4(b) and 4(c)]. Therefore, the internal high-microstrain due to the grain-to-grain contacts upon nonhydrostatic compression eventually promotes the cubic-to-monoclinic structural phase transition at a relatively low pressure of ~ 8.9 GPa.

However, after annealing the metastable m-Sc_2O_3 specimen at 1123 K and 9.0 GPa, we found that it reconstructed and transformed back to the cubic c-Sc_2O_3 [Figs. 3(a) and 3(b)]. Fitting the current x-ray diffraction pattern of the back-transformed c-Sc_2O_3 nanocrystals to the Williamson-Hall equation [30,31] yields the apparent microstrain of $\sim 0.61\%$ and the grain/crystallite size of $\sim 20(3)$ nm [see Fig. 4(c)]. This apparent strain (nonuniformed strain) derived from the peak broadening is different from the regular strains (uniform strain) expressed as $\Delta V/V$ usually obtained from the peak shift of x-ray diffraction patterns. Figure 4(d) shows the variation in d-spacing ratio of c-Sc_2O_3 as a function of pressure, together with those for m-Sc_2O_3 at 12.3 GPa and the reconstructive c-Sb_2O_3 at 1123 K and 9.0 GPa. At the low pressure range, the $d_{(440)}/d_{(222)}$ increases linearly with pressures and deviates from the linear relationship in the subsequent transition zone, whereas the $d_{(602)}/d_{(401)}$ for high-pressure m-Sc_2O_3 phase at 12.3 GPa is obviously lower than that at 11.2 GPa because of the strain/stress relaxation during the structural phase transition, and then probably exhibits a decreased trend with pressures.

To further confirm the microstrain-promoted structural evolution and phase instability of c-Sc_2O_3 at high pressure, we have performed Raman spectroscopy measurements on c-Sc_2O_3 at pressures up to ~ 42.5 GPa without the use of a pressure-transmitting medium. The *in situ* Raman spectrum of c-Sc_2O_3 at ambient conditions is shown in Supplemental Material, Section II (SII) [32], in which the respective Raman modes are indexed. An irreducible representation of the optical and phonon modes is described as $\Gamma = 4A_g + 5A_u + 4E_g + 5E_u + 14F_g + 17F_u$, where A_g, E_g, and F_g are Raman-active, F_u is infrared-active, and A_u and E_u are inactive [29,33].

For comparison, the representative Raman spectra of c-Sc_2O_3 at various pressures upon nonhydrostatic compression are shown in the Supplemental Material, Section II (SII)

[32]. We clearly find that the strongest Raman mode for the c-Sc_2O_3 is centered at $418\,cm^{-1}$ and is assigned as the F_g mode, which is more sensitive to the changes in the Sc-O chemical bonding upon nonhydrostatic compression, indicating a large polarizability change during the vibration [9]. To see closely into the structural stability in c-Sc_2O_3 under high pressure, Raman mode frequencies of c-Sc_2O_3 as a function of pressure are plotted in the Supplemental Material, Section II (SII) [32]. It is clearly found that most of the Sc-O mode frequencies increase monotonically with pressures or shift to high frequencies with pressures up to $\sim 42.5\,GPa$ in the Supplemental Material, Section II (SII) [32], except the appearance of apparent discontinuities in A_g ($494\,cm^{-1}$) and F_g ($524\,cm^{-1}$) modes at $\sim 9.3\,GPa$ and a pronounced Raman mode softening in F_g ($189\,cm^{-1}$) at pressures above $\sim 23\,GPa$. We propose the reason for the increase of vibrational mode frequencies with pressures is attributed to the contraction of the Sc-O bond upon compression, whereas the existence of the softening mode might be due to the proposed structural instability or phase transition in c-Sc_2O_3 upon nonhydrostatic compression. Meanwhile, the pronounced discontinuity at $\sim 9.3\,GPa$ for A_g ($494\,cm^{-1}$) and F_g ($524\,cm^{-1}$) modes, as shown in the Supplemental Material, Section II (SII) [32], is also probably due to the existence of the pressure-induced phase transition (without the information about the crystal symmetry) in c-Sc_2O_3 as observed in the *in situ* x-ray diffraction in Figs. 2 and 3(a).

To further unravel the microstrain effect on the structural stability of Sc_2O_3, we have performed first-principles calculations of the acoustic velocities, Poisson's ratio, and density of cubic c-Sc_2O_3 under high pressure, as shown in the Supplemental Material, Section III (SIII) [32]. Clearly, the density of c-Sc_2O_3 exhibits a monotonic increase with increasing pressure, in contrast to a pronounced anomaly in acoustic velocities (especially for the shear wave velocities) and Poisson's ratio at pressures of around 10–15 GPa, further supporting our experimentally observed results from our x-ray diffraction and Raman spectroscopy measurements. As shown in Fig. 2 and the Supplemental Material, Section II (SII) [32], we find that our x-ray observed transition pressure of $\sim 8.9\,GPa$ is in good agreement with that of $\sim 9.3\,GPa$ from our experimental Raman spectroscopy measurements, but significantly lower than those of 28–36 GPa from previously DAC-based hydrostatic compression experiments [9,10]. This discrepancy is attributed to the existence of internal microscopic stress and/or high-stress concentration in the specimen caused by grain-to-grain contacts upon nonhydrostatic compression, resulting in the promotion of the cubic-to-monoclinic structural transition or lowering of the transition pressure.

In addition to the high P-T structural stability, the thermoelastic properties of c-Sc_2O_3 are important parameters in understanding its comprehensive physical properties. The pressure-volume-temperature (P-V-T) relations of c-Sc_2O_3 based on the current synchrotron x-ray diffraction measurements are shown in Fig. 5(a). Fitting the entire current P-V-T data of c-Sc_2O_3 to the third-order high-temperature Birch-Murnaghan EOS [18], we obtained the bulk modulus of $B_{T0} = 184(2)\,GPa$ and $V_0 = (954.98 \pm 0.13)\,Å^3$ with the fixed $B' = $
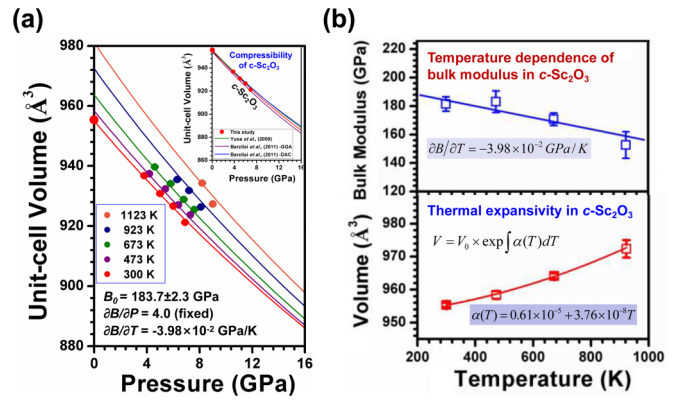
FIG. 5. (a) P-V-T relations of c-Sc_2O_3 obtained from the current experiments (denoted in different color circles). The isothermal compression curves at various temperatures (in different color curves) are calculated by the third-order high-temperature Birch-Murnaghan equation of state (EOS) with the derived thermoelastic properties of c-Sc_2O_3. Comparison of room-temperature P-V relations in c-Sc_2O_3 is shown as an inset. (b) The isothermal bulk modulus as a function of temperature (top); the bulk moduli at ambient pressure and various temperatures are derived by fitting the current P-V data to the third-order Birch-Murnaghan EOS with a fixed $\partial B/\partial P = 4.0$, yielding $\partial B/\partial T = -3.98 \times 10^{-2}\,GPa/K$. The unit-cell volume of c-Sc_2O_3 as a function of temperature (bottom), as described by $V = V_0 \int \alpha(T)dT\,(Å^3)$, where the volumetric thermal expansivity at ambient pressure is $\alpha(T) = 0.61 \times 10^{-5} + 3.76 \times 10^{-8}T$ (K). The unit-cell volumes at atmospheric pressure and various temperatures are derived by fitting the present P-V data to the third-order Birch-Murnaghan EOS with a fixed $\partial B/\partial P = 4.0$.

4.0. The obtained B_{T0} from our robust high P-T synchrotron x-ray diffraction data is well consistent with the reported values of $B_{T0} = 189(7)\,GPa$ [12] and $191(11)\,GPa$ [17] within the mutual uncertainties from room-temperature DAC experiments, but is $\sim 5\%$ larger than the theoretical result by Barzilai *et al.* [17]. For good understanding, the room-temperature P-V relations in c-Sc_2O_3 compared with previous studies [12,17], are shown here as an inset. Moreover, the temperature dependence of bulk modulus, $(\partial B_0/\partial T)_P$ was determined for the c-Sc_2O_3 and was found to be $-3.98 \times 10^{-2}\,GPa/K$ [top: Fig. 5(b)]. The volumetric thermal expansivity of c-Sc_2O_3 at ambient pressure is determined to be $\alpha(T) = 0.61 \times 10^{-5} + 3.76 \times 10^{-8}\,T$ (K) [bottom: Fig. 5(b)].

IV. CONCLUSIONS

In summary, structural stability and thermoelasticity of c-Sc_2O_3 nanocrystals have been studied by synchrotron x-ray diffraction at simultaneously high P-T conditions, complemented with high-pressure Raman spectroscopy measurements and first-principles DFT calculations. Here, we reported an irreversible structural transformation in Sc_2O_3 nanocrystals from the cubic structure to a monoclinic phase which occurred at pressures above $\sim 8.9\,GPa$ upon nonhydrostatic compression. This pressure-induced structural instability or phase transition is further confirmed by our experimental high-pressure Raman spectroscopy measurements and

theoretical calculations. Interestingly, the critical transition-pressure (P_{tr}) of ~8.9 GPa is significantly lower than the previous results of 28–36 GPa under DAC-based hydrostatic compression. We propose this lowering P_{tr} is attributed to the existence of internal microscopic stress or high-stress concentration in the specimen caused by grain-to-grain contacts upon nonhydrostatic compression. On the other hand, the formed monoclinic m-Sc_2O_3 new phase underwent a reversible reconstructive phase transition after annealing at ~1123 K and 9.0 GPa and transformed back to the cubic counterpart. These findings are not only of great importance for the understanding of the thermoelastic properties of Sc_2O_3, but also may have significant implications for the design of phase-switching devices and the exploration of the structural relationship among sesquioxides for their uses at extreme conditions.

[1] Z. Xu, A. Daga, and H. Chen, Microstructure and optical properties of scandium oxide thin films prepared by metalorganic chemical-vapor deposition, Appl. Phys. Lett. **79**, 3782 (2001).

[2] R. Krsmanović, O. I. Lebedev, A. Speghini, M. Bettinelli, S. Polizzi, and G. Van Tendeloo, Structural characterization and luminescence properties of nanostructured lanthanide-doped Sc_2O_3 prepared by propellant synthesis, Nanotechnology **17**, 2805 (2006).

[3] R. M. Jacobs, J. H. Booske, and D. Morgan, Electron emission energy barriers and stability of Sc_2O_3 with adsorbed Ba and Ba-O, J. Phys. Chem. C **118**, 19742 (2014).

[4] V. Grover, R. Shukla, D. Jain, S. K. Deshpande, A. Arya, C. G. S. Pillai, and A. K. Tyagi, Complex $GdSc_{1-x}In_xO_3$ oxides: Synthesis and structure driven tunable electrical properties, Chem. Mater. **24**, 2186 (2012).

[5] H. R. Hoekstra and K. A. Gingerich, High-pressure B-type polymorphs of some rare-earth sesquioxides, Science **146**, 1163 (1964).

[6] M. Zinkevich, Thermodynamics of rare earth sesquioxides, Prog. Mater. Sci. **52**, 597 (2007).

[7] X. Yan, X. Ren, D. He, B. Chen, and W. Yang, Mechanical behaviors and phase transition of Ho_2O_3 nanocrystals under high pressure, J. Appl. Phys. **116**, 033507 (2014).

[8] F. Weigel and V. Scherer, Die chemie des promethiums II. Die polymorphie des promethium (III)-oxids, Radiochim. Acta **4**, 197 (1965).

[9] D. Liu, W. Lei, Y. Li, Y. Ma, J. Hao, X. Chen, Y. Jin, D. D. Liu, S. Yu, Q. Cui, and G. Zou, High-pressure structural transitions of Sc_2O_3 by x-ray diffraction, Raman spectra, and *ab initio* calculations, Inorg. Chem. **48**, 8251 (2009).

[10] S. V. Ovsyannikov, E. Bykova, M. Bykov, M. D. Wenz, A. S. Pakhomova, K. Glazyrin, H.-P. Liermann, and L. Dubrovinsky, Structural and vibrational properties of single crystals of scandia, Sc_2O_3 under high pressure, J. Appl. Phys. **118**, 165901 (2015).

[11] Q. Zhang, J. Yang, X. Wu, and S. Qin, Phase stability and elasticity of Sc_2O_3 at high pressure, Eur. Phys. J. B **84**, 11 (2011).

[12] A. F. Reid and A. E. Ringwood, High-pressure scandium oxide and its place in the molar volume relationships of dense structures of M_2X_3 and ABX_3 type, J. Geophys. Res. **74**, 3238 (1969).

[13] H. Yusa, T. Tsuchiya, N. Sata, and Y. Ohishi, High-pressure phase transition to the Gd_2S_3 structure in Sc_2O_3: A new trend in dense structures in sesquioxides, Inorg. Chem. **48**, 7537 (2009).

[14] T. Atou, K. Kusaba, K. Fukuoka, M. Kikuchi, and Y. Syono, Shock-induced phase transition of M_2O_3 (M = Sc, Y, Sm, Gd, and In)-type compounds, J. Solid State Chem. **89**, 378 (1990).

[15] V. I. Aleksandrov, V. F. Kitaeva, V. V. Osiko, N. N. Sobolev, V. M. Tartarintsev, and I. L. Chistyi, Spectra of molecular scattering of light in Y_2O_3 and Sc_2O_3 crystals, Sb. Kratk. Soobshch. Fiz. AN SSSR Fiz. Inst. P. N. Lebedeva, No. **4**, 8 (1976) [Sov. Phys. Lebedev. Inst. Rep. No. **4**, 7 (1976)].

[16] S. L. Dole Jr., O. Hunter, and F. W. Calderwood, Elastic properties of polycrystalline scandium and thulium sesquioxides, J. Am. Ceram. Soc. **60**, 167 (1977).

[17] S. Barzilai, I. Halevy, and O. Yeheskel, Bulk modulus of Sc_2O_3: *Ab initio* calculations and experimental results, J. Appl. Phys. **110**, 043532 (2011).

[18] Y. Zou, X. Qi, X. Wang, T. Chen, X. Li, D. Welch, and B. Li, High-pressure behavior and thermoelastic properties of niobium studied by *in situ* x-ray diffraction, J. Appl. Phys. **116**, 013516 (2014).

[19] B. Li, J. Kung, T. Uchida, and Y. Wang, Pressure calibration to 20 GPa by simultaneous use of ultrasonic and x-ray techniques, J. Appl. Phys. **98**, 013521(2005).

[20] Y. Wang, M. Rivers, S. Sutton, N. Nishiyama, T. Uchida, and T. Sanehira, The large-volume high-pressure facility at GSE-CARS: A "swiss-army-knife" approach to synchrotron-based experimental studies, Phys. Earth Planet. Inter. **174**, 270 (2009).

[21] A. Le Bail, H. Duroy, and J. L. Fourquet, *Ab initio* structure determination of $LiSbWO_6$ by x-ray powder diffraction, Mater. Res. Bull. **23**, 447 (1988).

[22] H. Toby, EXPGUI, a graphical user interface for GSAS, J Appl. Cryst. **34**, 210 (2001).

[23] D. L. Decker, High-pressure equation of state for NaCl, KCl, and CsCl, J. Appl. Phys. **42**, 3239 (1971).

[24] H.-K. Mao, P. M. Bell, J. W. Shaner, and D. J. Steinberg, Specific volume measurements of Cu, Mo, Pd, and Ag and

calibration of the ruby R1 fluorescence pressure gauge from 0.06 to 1 Mbar, J. Appl. Phys. **49**, 3276 (1978).

[25] D. Vanderbilt, Soft self-consistent pseudopotentials in a generalized eigen-value formalism, Phys. Rev. B **41**, 7892 (1990).

[26] J. P. Perdew, K. Burke, and M. Ernzerhof, Generalized Gradient Approximation Made Simple, Phys. Rev. Lett. **77**, 3865 (1996).

[27] M. Parrinello and A. Rahman, Polymorphic transitions in single crystals: A new molecular dynamics method, J. Appl. Phys. **52**, 7182 (1981).

[28] M. C. Payne, M. P. Teter, D. C. Allen, T. A. Arias, and J. D. Joannopoulos, Iterative minimization techniques for *ab initio* total-energy calculations: Molecular dynamics and conjugate gradients, Rev. Mod. Phys. **64**, 1045 (1992).

[29] N. D. Todorov, M. V. Abrashev, V. Marinova, M. Kadiyski, L. Dimowa, and E. Faulques, Raman spectroscopy and lattice dynamical calculations of Sc_2O_3 single crystals, Phys. Rev. B **87**, 104301 (2013).

[30] Y. Zhao, J. Zhang, B. Clausen, T. D. Shen, G. T. Gray, and L. Wang, Thermomechanics of nanocrystalline nickel under high pressure-temperature conditions, Nano Lett. **7**, 426 (2007).

[31] Y. Wang, J. Zhang, and Y. Zhao, Strength weakening by nanocrystals in ceramic materials, Nano Lett. **7**, 3196 (2007).

[32] See Supplemental Material at http://link.aps.org/supplemental/10.1103/PhysRevB.102.214115 for the description of the three sections. Section I (SI): SEM characterizations, Section II (SII): High-pressure Raman spectroscopy measurements, Section III (SIII): First-principles theoretical calculations.

[33] M. V. Abrashev, N. D. Todorov, and J. Geshev, Raman spectra of R_2O_3 (R-rare earth) sesquioxides with C-type bixbyite crystal structure: A comparative study, J. Appl. Phys. **116**, 103508 (2014).